Materials Chemistry and Physics 249 (2020) 122967

Contents lists available at ScienceDirect

Materials Chemistry and Physics

journal homepage: www.elsevier.com/locate/matchemphys

Charge transfer in Pr-Doped cerium oxide: Experimental and theoretical investigations

Regiane Cristina de Oliveira [a,b,*,1], Luis Cabral [c], Ana Cristina Cabral [d], Priscila Barros Almeida [e], Nicolas Tibaldi [f], Julio Ricardo Sambrano [b], Alexandre Zirpoli Simões [a], Carlos Eugenio Macchi [g], Francisco Moura [d], Gilmar Eugenio Marques [c], Miguel Adolfo Ponce [f], Elson Longo [e]

[a] Faculty of Engineering of Guaratinguetá, São Paulo State University – UNESP, Guaratinguetá, SP, Brazil
[b] Permanent Address:Modeling and Molecular Simulations Group, São Paulo State University, UNESP, Bauru, SP, Brazil
[c] Department of Physics, Federal University of Sao Carlos, 13565-905, São Carlos, SP, Brazil
[d] Laboratório Interdisciplinar de Materiais Avançados, Universidade Federal de Itajubá, Unifei – Campus, Itabira, MG, Brazil
[e] CDMF, LIEC, Chemistry Department of the Federal University of São Carlos - (UFSCar), P.O. Box 676, 13565-905, São Carlos, SP, Brazil
[f] Institute of Materials Science and Technology (INTEMA), University of Mar del Plata and National Research Council (CONICET), Juan B. Justo 4302, B7608FDQ, Mar del Plata, Argentina
[g] Instituto de Física de Materiales Tandil, UE CIFICEN (CONICET- Consejo Nacional de Investigaciones Científicas y Técnicas-CONICET), Pinto 399, B7000GHG, Tandil, Argentina

HIGHLIGHTS

- CeO_2 doped with Pr were obtained by microwave-assisted hydrothermal method.
- CeO_2:Pr nanopowders heat treated in O_2, CO, and *vacuum* formed distinct amount of vacancies.
- The vacancies formations are study by PALS and PL techniques.
- The electrical measurements demonstrated that CeO_2:Pr acts as n-type semiconductor.
- DFT calculates revealed the presence of Pr states in the 4f states of Ce atoms.

GRAPHICAL ABSTRACT

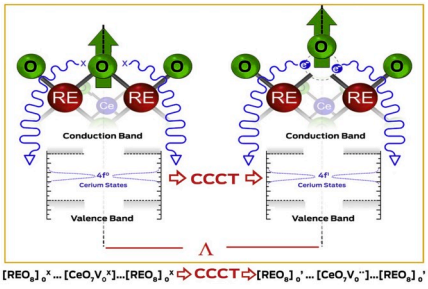

ARTICLE INFO

Keywords:
CeO_2-Pr
Defects
Positron annihilation lifetime spectroscopy
Photoluminescence
Density functional theory

ABSTRACT

In this study was synthesized cerium oxide (CeO_2) doped with praseodymium (Pr) using a microwave-assisted hydrothermal method. The positions of the vacancies with respect to Ce^{3+}/Ce^{4+} and the vacancy-like defects surrounded by the electronic density of Pr atoms were determined through photoluminescence (PL) measurements, positron annihilation lifetime spectroscopy, and density functional theory (DFT). Distinct PL responses were observed for Pr-doped CeO_2 indicating that oxygen vacancies contribute to the formation of deep energy levels in the forbidden region, thus facilitating charge transfer. The interplay between the experimental measurements and computational simulations at the microscopic level based on DFT revealed the charge rearrangement in oxygen-deficient CeO_2:Pr systems. These results indicate that oxygen vacancies and electrons at the 4f states contribute to electrical conduction, thereby demonstrating that Pr-doped CeO_2 acts as an n-type semiconductor.

* Corresponding author. Faculty of Engineering of Guaratinguetá, São Paulo State University – UNESP, Guaratinguetá, SP, Brazil.
E-mail addresses: g.ianeoliveira@hotmail.com, re260389@gmail.com (R. Cristina de Oliveira).
[1] Modeling and Molecular Simulations Group, São Paulo State University, UNESP, Bauru, SP, Brazil.

https://doi.org/10.1016/j.matchemphys.2020.122967
Received 5 December 2019; Received in revised form 25 March 2020; Accepted 26 March 2020
Available online 31 March 2020

1. Introduction

Over the past few decades, nanostructured metal oxides have been extensively studied by researchers in multidisciplinary fields. In particular, cerium dioxide (CeO_2) is an n-type semiconductor with the structure and space group of fluorite (Fd-3m), where in cerium atom is surrounded by eight oxygen atoms in a cubic face-centered arrangement [1]. These structural features facilitate the incorporation of dopants into the host matrix, a method widely used to shape and extend the optical and electrical properties of these materials [2]. In our previous work [3], we reported the development of nanostructured CeO_2 that exhibited dual gas sensing behavior (electric and optical) when doped with lanthanum and exposed to a carbon monoxide (CO) atmosphere at temperatures above 350 °C. This behavior was attributed to the itinerant 4f electrons introduced by the generation of oxygen vacancies. Therefore, oxygen vacancies play an essential role in this important oxide material. However, very few studies been conducted to generate these favorable defects and understand their roles in the activity of nanostructured CeO_2 at the atomic level. The most significant properties affected by doping CeO_2 with rare-earth (RE) elements are the rapid changes observed in electrical and optical responses, in contrast to pure CeO_2, which gave rise to the electrical behavior with a response time of 54 s, which is not efficient enough for sensor applications. Thus, the vacancy structures of these oxides should be studied using a probe that can provide information at the atomic level. Positron annihilation lifetime spectroscopy (PALS) is a well-recognized technique for studying defect structures in solids because of the tendency of positrons to become localized and annihilated at sites with lower than average electronic density. These sites, which act as positron traps, are defects with a specific open volume. This non-destructive technique can give information regarding the size, type, and relative concentration of different open-volume defects at the ppm level [4].

The use of RE elements as dopants has been extensively discussed, and previous studies have reported that the doping of CeO_2 with these elements facilitates the formation of anionic vacancies, which changes the electrical conductivity and increases the formation of surface defects, thereby contributing significantly to the catalytic activity [5–8]. A previous study has highlighted the fact that the addition of a trivalent cation to the lattice promotes the creation of a higher number of oxygen vacancies and reduces the difference between the Fermi level energy and the valence band energy (E_F-E_V). These two phenomena can have opposite effects on the final electrical resistance of the material, with the vacancy generation increasing the number of electrons in 4f states as well as conductivity. In contrast, if the Fermi level (E_F) is stabilized, the E_{4f}-E_F energy gap increases, and the conductivity of the sample decreases. This phenomenon was observed in a europium-doped CeO_2 sample that presented a slightly lower band gap value of 3.26 eV, thereby becoming less conductive than a pure CeO_2 sample [9].

The electrical properties of CeO_2 are dependent on the reduction of Ce^{4+} to Ce^{3+}. Dhara et al. [10] showed the effect of this redox property on the charge transfer gap between the O (2p) and Ce (4f) states, observing a blue shift in the absorption spectrum of CeO_2 nanocrystals. Additionally, Abbas et al. [11] showed that the narrowing of this band gap energy can be achieved by increasing the number of oxygen vacancies in the structure by systematically doping the CeO_2 nanoparticles with Mn through synthetization by the co-precipitation method.

A survey on the literature shows that the development and use of pure and doped ceria-based nanostructured materials have gained considerable attention. Doping with other RE elements, such as praseodymium or gadolinium, creates oxygen vacancies that facilitate the migration of oxygen ions through the lattice [12]. Pr has some properties that mimic those of Ce. Both Ce and Pr can form cations with 3+ and 4+ oxidation states with very similar cation sizes (0.97 and 0.96 Å for Ce^{4+} and Pr^{4+}, and 1.14 and 1.13 Å for Ce^{3+} and Pr^{3+}, respectively). Consequently, the high solubility of Ce and Pr cations allows the formation of a solid solution with very intriguing properties [13].

Therefore, in this study, we report the synthesis and characterization of Pr-doped cerium oxide with concentrations of 4, 8, and 12 mol % by using a microwave-assisted hydrothermal (MAH) method. The obtained samples were subjected to thermal treatments in three different atmospheres, i.e., CO, O_2, and *vacuum*. The main objective of such substitution is to create electronic defects that are responsible for changes in the optical, sensing, and structural properties of CeO_2-based materials.

Among the several properties of pure or doped CeO_2 nanoparticles, photoluminescence (PL) has been widely investigated [14–19]. PL emission is closely related to the crystal structure and the corresponding distorted metal-oxygen polyhedral. A comparison of the results of different studies is complicated because different syntheses produce particles with different exposed surface or bulk defects, oxygen vacancies, and ratios of reduced Ce^{3+}. Accordingly, the combined analysis of the results of density functional theory (DFT) and experimental methods such as PL, positron annihilation, and electrical conduction measurements can facilitate a deeper understanding of the behavior of defective CeO_2 systems in different atmospheres. Thus, the main objective of this study is to investigate the influence of oxygen vacancies on the PL and PAL spectra of CeO_2 nanoparticles when doped with different amounts of Pr. These interactions are discussed in terms of the phenomena involved in the substitution of Pr^{3+} ions in the CeO_2 host lattice and the resulting changes in the structural, morphological, vibrational, optical, and electrical properties determined by X-ray diffraction, PL, PALS, DC electrical measurements, and DFT calculations.

2. Experimental section

2.1. Synthesis and characterization of nanopowders

The experimental procedure used for preparing Pr-doped CeO_2 was based on the dissolution of ammonium cerium (IV) nitrate (99.0%, Sigma) in an aqueous medium, followed by heating at 50 °C with constant stirring. Separately, Pr_2O_3 (99.9%, Aldrich) was dissolved in a nitric acid medium and added to the solution of Ce. The resulting mixture was heated at 70 °C with constant stirring, and its pH was adjusted through the addition of a basic aqueous solution of 2 M KOH (p. a., Synth) until the pH reached 10. The resulting solution was transferred into a sealed Teflon autoclave and placed in a domestic microwave (2.45 GHz, maximum power of 800 W). The reaction system was then heat-treated at 100 °C for 8 min with the heating rate fixed at 10 °C/min. The pressure in the sealed autoclave was stabilized at 1.2 atm. The resultant solution was transferred into centrifuge tubes and then subjected to three cycles of washing with deionized water at 2000 rpm for 10 min each. Subsequently, the obtained $Ce_{1-3/4x}Pr_xO_2$ nanoparticles were dried at 100 °C for 48 h in an oven. The synthesized $Ce_{1-3/4x}Pr_xO_2$ powders (doped with 4, 8, and 12% of Pr) were labeled as F4, F8, and F12, respectively.

2.2. Powder treatments and characterization under different atmospheres

Fractions of the synthesized powders (doped with 4, 8, and 12% of Pr), were thermally treated up to 330 °C for 1 h with a heating rate of 1 °C/min in different atmospheres. After heating in *vacuum*, CO (400 ppm), and dry air atmospheres, the samples were cooled down to room temperature. Further, three different thermal treatments were performed to obtain samples with different defective structures [20,21]. After the thermal treatments the nanopowders were also structurally characterized based X-ray powder diffraction (XRD) analysis recorded on the Rigaku-D/Max 2500 diffractometer (Japan) with graphite-mono chromatized Cu Kα radiation (λ = 0.15405 nm). Rietveld refinements of the measured XRD patterns recorded from 20° to 100° with a scanning velocity of 1 degmin^{-1} were conducted using the general structure analysis program (GSAS). UV–vis diffuse reflectance spectroscopy was conducted on a UV–visible spectrometer (Varian, model Cary 5G), and

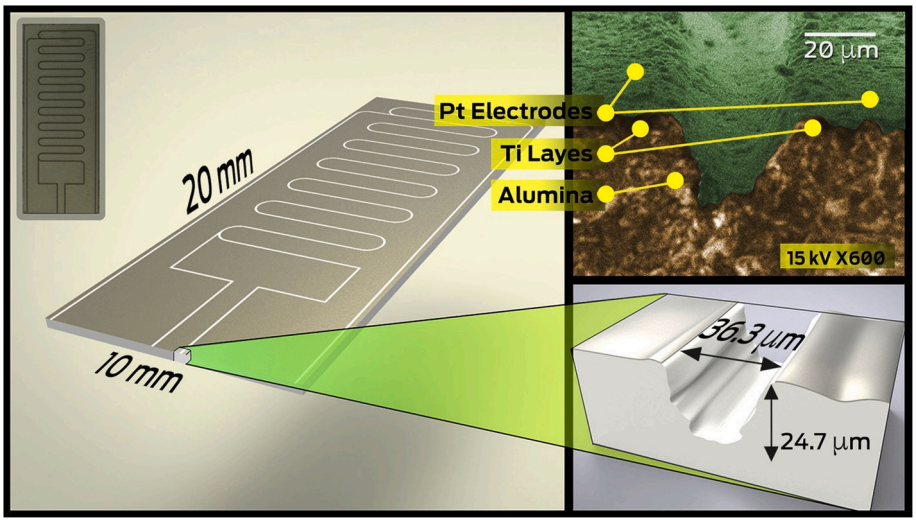

Fig. 1. Substrate with interdigitated electrodes deposited by a home-built micromachining laser along with a deposited thick film.

the spectra were taken in diffuse-reflectance mode. The morphologies of the samples were examined using scanning electron microscopy (SEM) (Supra 35-VP Carl Zeiss, Germany) operated at 15 kV. In addition, transmission electron microscopy (TEM), at 200 kV and energy-dispersive X-ray spectroscopy (EDS) mappig measurements were performed using a FEI microscope (model Tecnai G2 F20, USA). X-ray photoelectron spectroscopy (XPS) measurements were conducted by a Scienta Omicron ESCA + spectrometer system equipped with a hemispherical analyzer (EA125) and a monochromatic source of Al Kα ($h\nu = 1486.7$ eV). The C1s peak at a binding energy of 285 eV was used in the analysis as an energy reference. PALS measurements were performed in a fast-fast type spectrometer with collinear geometry and a time resolution of 210 ps. A 10 μCi sealed source of ^{22}NaCl deposited on two thin Kapton foils (7.5 μm thick) sandwiched between two identical samples was used as the positron source. The spectra were acquired at room temperature (RT), and 1.5–2 × 10^6 counts per spectrum were collected. After subtracting the background and source contribution, the positron lifetime spectra were analyzed using the LT10 code [22]. Generally, several lifetime components can be extracted from a PALS spectrum; each component is characterized by a positron lifetime value τ_i and an associated intensity I_i. The state *i* can be the delocalized state (bulk state) or a localized one at a defect site (such as vacancies and vacancy clusters) in which positrons can be trapped and annihilated. The value of τ_i indicates the type of defect, and it is a measure of the open volume associated with the defect that traps positrons. Larger τi values indicate that positrons are trapped in bigger defects. Furthermore, the associated intensity provides information regarding the defect density. The lifetime component values reported in this study for each sample represent an average of at least ten measurements under the same experimental conditions. The PL spectra were measured with a Monospec 27 monochromator (Thermal Jarrel Ash, United States) coupled to an R446 photomultiplier (Hamamatsu Photonics, Japan). A krypton ion laser (Coherent Innova 200 K, United States) was used as the excitation source.

2.3. Film conformation and characterization

Pastes were obtained based on a mixture of nanopowders (4, 8, and 12% Pr-doped CeO_2) and organic binder (glycerol). The pastes were used to prepare three thick porous films (F4, F8, and F12) employing the screen-printing technique on 96% dense insulating alumina substrates, on which a 25 nm titanium adhesion layer and a 200 nm platinum layer had been deposited by radio frequency-sputtering. The interdigitated platinum electrodes were delineated using a home-built micromachining laser. The dimensions of the substrate were 20 × 10 mm (length × width), and the Pt electrodes had a resistance of 10 Ω. The powder/binder ratio was set at 1.6 g/mL. After deposition, the films were heat-treated in a dry air atmosphere with the temperature increasing at a rate of 1 °C/min up to 380 °C, and they were held at this temperature for 2 h to allow the binder to evaporate. A deposited film is shown in Fig. 1.

The electrical resistance (above 400 °C) was measured as a function of time and temperature in *vacuum* and in dry air and CO atmospheres at constant pressures of 100 mmHg and 200 mmHg for all doped samples, respectively. The electrical measurements were conducted using an optoelectronic device (Patent INPI Argentina 201501039539/INPI Brazil 10 2016 028383 3) [23,24]. The optoelectronic characterization chamber consisted of a closed chamber in which three cycles of heating were performed in *vacuum* up to 400 °C before the resistance values were measured, thereby assuring no trace of any humidity. The measurements were made when the samples reached a steady state, and no changes in resistance were observed over time, with an applied excitation current of 1 mA, which was applied using the two-wire technique with a DC-type measurement. An Agilent 3440 A multimeter was used for the electrical resistance measurements.

3. Theoretical approach and computational details

A deep understanding of the Ce and Pr oxidation states and the local magnetic moment can be obtained by performing calculations at the atomic level based on DFT [25,26]. A better investigation of the electronic structure was achieved by using the semi-local Perdew–Burke–Ernzerhof exchange [27] exchange and correlation energy functional within the spin-polarized generalized gradient approximation (GGA) formulation. The Kohn–Sham equations were solved by using the all-electron projector augmented wave (PAW) method [28,29], employing the Ce ($4f^1$, $5\,d^1$, $6s^2$), O ($2s^2$,$2p^4$), and Pr ($4f^3$, $6s^2$) PAW projectors, where the valence states are shown in the parenthesis, as implemented in the Vienna *ab initio* simulation package (VASP), version 5.4.4 [30,31]. The stress tensor calculation was performed by using a plane-wave basis extension with a cutoff of 829 eV; meanwhile, for atomic force optimization, a plane wave basis with a cutoff of 466 eV was used, which is 12.5% higher than that recommended by the VASP package. The integration of the Brillouin zone was performed by using a 2 × 2 × 2 k-mesh for the stress tensor and atomic force optimization, while twice that was used for the electronic properties. A Gaussian smearing of 0.01 eV was employed in all calculations, and the adopted stop criterion for self-consistency in the calculation was reached when

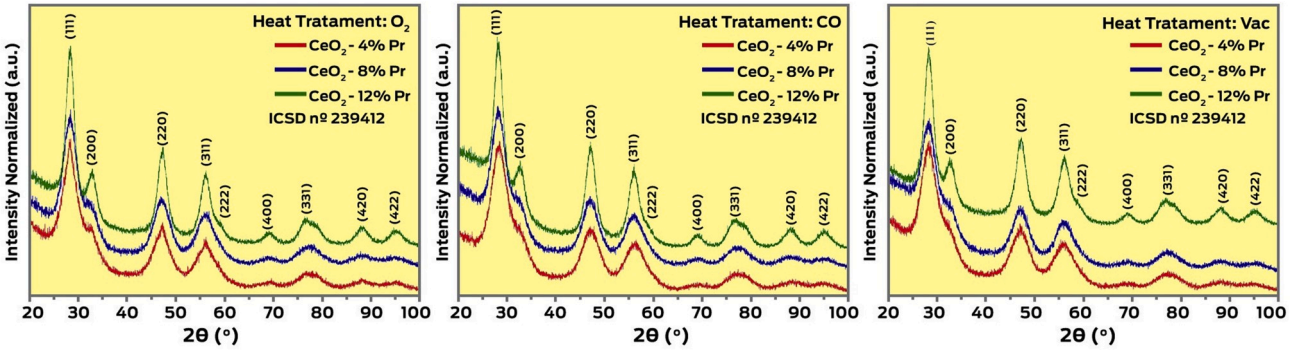

Fig. 2. XRD patterns of CeO_2 doped with 4, 8, and 12% Pr, and subjected to heat treatment in O_2 and CO atmospheres, and in *vacuum*.

the forces in all atoms were smaller than 0.01 eV/A. For the large CeO_2 band gap calculation, the Hubbard correction (GGA + U) method proposed by Dudarev et al. [32] was adopted, where the U parameters were 4.0, 5.0, and 5.5 eV for the f-Pr, f-Ce, and p-O states, respectively, according to Refs. [33–37].

4. Results and discussion

4.1. XRD patterns and Rietveld refinement

Fig. 2 shows the XRD patterns of CeO_2 doped with 4, 8, and 12% Pr and subjected to heat treatment in O_2 and CO atmospheres and in vacuum. All patterns were similar and characteristic of the cubic phase with space group "Fm-3m." All the diffraction peaks agreed with the inorganic crystal structure database (ICSD) pattern no. 239412, suggesting

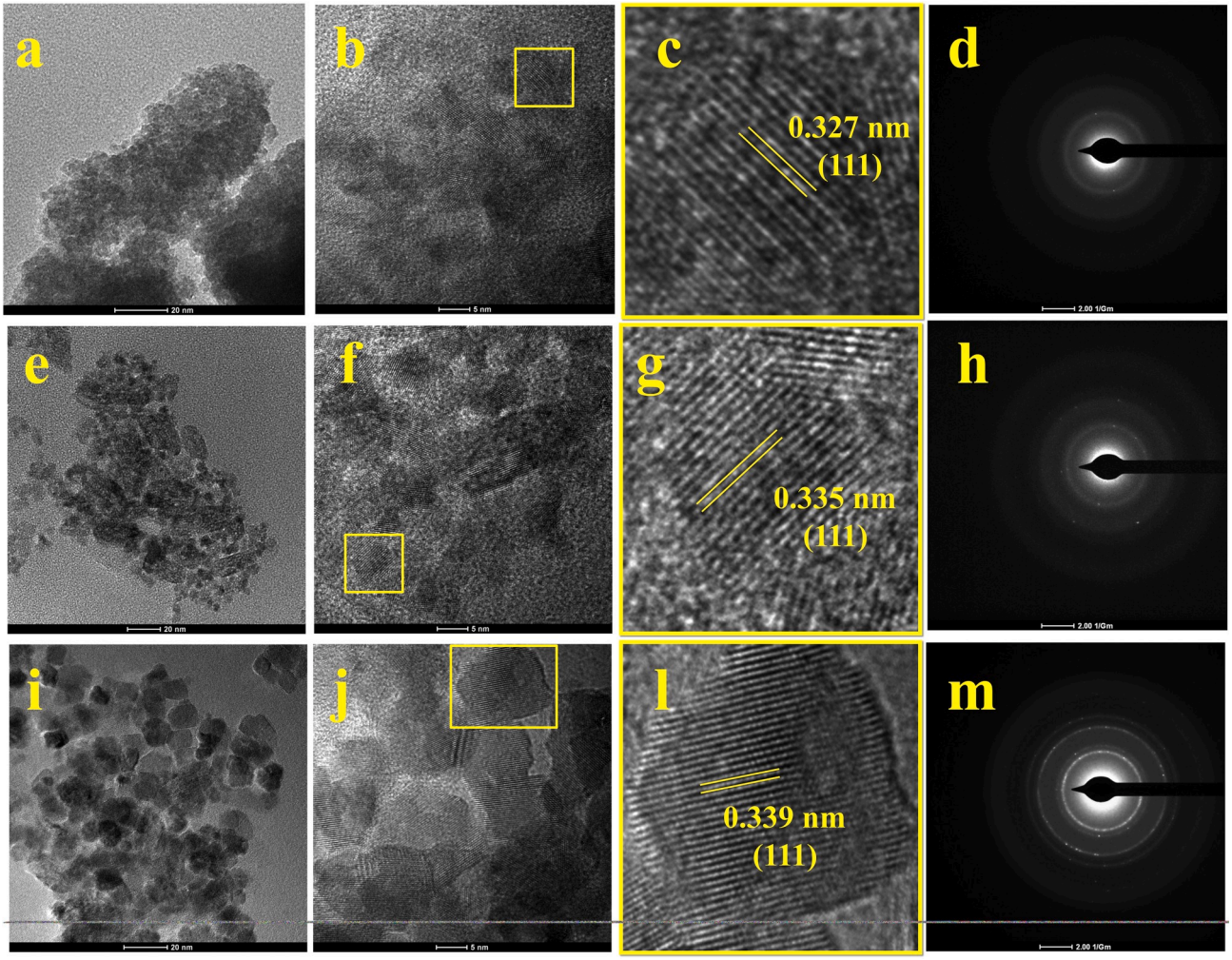

Fig. 3. Low magnification TEM image of CeO_2 doped with 4 (a, b), 8 (e, f) and 12% (i, j) of Pr. Zoom in the yellow square region in the HRTEM image of CeO_2 doped with 4 (c), 8 (g) and 12% (l) of Pr. SAED patterns of CeO_2 doped with 4 (d), 8 (h) and 12% (m) of Pr. (For interpretation of the references to color in this figure legend, the reader is referred to the Web version of this article.)

high-phase purity. The absence of peaks other than those of CeO_2 in the XRD patterns of the synthesized samples confirms the successful substitution of Pr ions into the sites of Ce ions in the CeO_2 lattice.

We characterized the crystalline structure in detail by determining the structural (e.g., cell parameters, site occupancy, atomic positions) and microstructural parameters (e.g., crystallite size, microstrain) using the Rietveld refinement method. The results obtained by employing the Rietveld method are shown in Fig. S1 and Table S1. The fitting parameters w*R* indicated good agreement between the calculated and observed XRD patterns for the as-prepared CeO_2 nanocrystals in this study. Moreover, the lattice parameters (*a, b, c*) and bond angle, which were estimated from the refinement confirmed the cubic structure.

4.2. Morphological analysis

By means of the SEM images (Fig. S2), it can be observed that the CeO_2-Pr powders synthesized by the MAH method in different times of synthesis, present a size range of the order of a few nanometers, highly agglomerated. It was not possible to observe significant differences in size and morphology of the CeO_2 particles doped with different amount of Pr, due this, the morphology and crystallinity of the samples were examined by TEM analyses. TEM images of CeO_2 nanocrystals obtained at different Pr contents are shown in Fig. 3 (a) for CeO_2-4% Pr, (e) for CeO_2-8% Pr and (i) for CeO_2-12% Pr synthesized by MAH under KOH at 100 °C for 8 min, revealing the particle sizes are approximately range from 5 to 15 nm with uniform size distribution. According to the image, most of the particles of CeO_2 nanoparticles are homogeneous with an average particle size increase as nominal Pr content increases. CeO_2-4% Pr powders display poor contrast and intense agglomeration amongst extremely fine particles, these particles present size range from 5 to 7 nm. For the CeO_2-8% Pr powders, the nanocrystals were relatively spherical with low uniform and size distribution from 7 to 12 nm. With the increase in the concentration of Pr to form CeO_2-12% Pr powders, the nanocrystals became more organized, with a slight formation of defined faces. Also, it can be seen that the size of the particle distribution increased from 12 to 15 nm. Fig. 3 (b, f, j) and the zoom done in the region indicated by the yellow square (c, g, l) illustrate HRTEM images for the CeO_2 doped with 4, 8, and 12% Pr, respectively, where it is possible to see an interplanar distance of 0.327, 0.335, and 0.339 nm, for the CeO_2 doped with 4, 8, and 12% Pr samples respectively, corresponding to the (111) plane, attesting the cubic phase with space group "Fm-3m." (ICSD no. 239412). Furthermore, selected area electron diffraction (SAED) patterns images are presented in Fig. 3 d, h and m, for the CeO_2 doped with 4, 8, and 12% Pr samples respectively, where can be observed that the intensity on the reflection patterns enhanced with the Pr content increases on the CeO_2 samples. These results indicating that the particle's morphology, size, and crystallinity of the CeO_2-Pr doped samples changes with the increase in the concentration of Pr. Therefore, we can point out that the Pr atoms affects the order/disorder relation of the CeO_2 and modifies the of oxygen vacancies concentration (as observed by XPS analyses (Fig. S5 in the SI). This fact contributes to elucidate the effect of Pr in the sensing and electric properties.

Table 1
Characteristic positron lifetimes and their associated intensities (I_1 (%) = 100 − I_2) obtained from the decomposition of the PALS spectra for the F4, F8, and F12 samples thermally treated under different atmospheres.

Samples	Atmospheres	τ_1(ps)± 1 ps	τ_2(ps)± 2 ps	I_2 (%)± 0.5%
F_4	O_2	189	367	52.3
F_4	CO	198	373	57.1
F_4	Vac	191	370	56.5
F_8	O_2	193	363	54.4
F_8	CO	202	375	58.4
F_8	Vac	200	374	58.2
F_{12}	O_2	198	370	58.0
F_{12}	CO	206	376	60.0
F_{12}	Vac	205	374	60.0

4.2.1. PALS results

PALS spectra obtained in this study were satisfactorily fitted by considering three-lifetime components. All measured spectra showed the presence of an almost constant long-lived lifetime of 2000 ± 200 ps with a small associated intensity (<2%). This lifetime component corresponds to ortho-positronium formation in the inter-rain spacing. Due to its small contribution to the PALS spectra, this lifetime component was not considered during the positron result analysis.

The values of the positron lifetime parameters obtained from the decomposition of PALS spectra are presented in Table 1. The first lifetime component (τ_1) has values ranging from 189 to 206 ps, while the second lifetime component (τ_2) in all cases is higher than 360 ps, with an associated intensity higher than 50%. It is worth noting that in nanostructured materials, such as the system studied in this work, nanocrystals present a particle size that is smaller than the typical positron diffusion length in solids, L_+∼50–100 nm. In this case, it can be assumed that the majority of the thermalized positrons inside the grains can reach the grain boundaries (GB) by diffusion. Furthermore, positrons can be used to probe defects with an open volume comparable to the small vacancy clusters located at the GBs [38].

Recently, several researchers have used PALS to characterize changes in the defect structures of different CeO_2-based nanostructured systems resulting from changes in the synthesis process [39–41] or in the dopant type and concentration [42,43]. In all cases, researchers have reported the presence of one lifetime component with values between 300 and 450 ps and a shorter one with values between 230 and 277 ps. These researchers attributed the longer lifetime component to positron annihilation in the larger surface oxygen vacancy-clusters (VCs), while the shorter component is attributed to positron annihilation in the small neutral Ce^{3+}-oxygen vacancy associations. In doped CeO_2 systems, doping can also play a role in the above-mentioned vacancy-like associations. It is worth noting that isolated oxygen vacancies are not effective trapping centers for positrons because they are positively charged; thus, they repel positrons. However, the above-mentioned researchers proposed that the association between a positive oxygen vacancy and an adjacent RE^{3+} ion at a Ce^{4+} site that carries an effective negative charge will render such an association neutral, making it an effective positron trap.

Accordingly, it is reasonable to assume from the τ_2 values presented in Table 1 that the clusters revealed in our samples contain VCs, including Ce^{3+} and Pr^{3+} metal ions. Moreover, the measured values of τ_1 are systematically higher than the value reported in the literature for the free-defect CeO_2 phase, τ_b = 187ps [42,43]. This result indicated that the short-lived lifetime corresponds to a mixed state. The τ_1 value represents contributions from positron annihilation events in small open volume defects and the reduced bulk positron lifetime. In such a case, the small open volume defects can be the above-mentioned small neutral Ce^{3+}-oxygen vacancies and/or Pr^{3+}-oxygen vacancy associations, located either at the GBs or inside the nanoparticles as structural defects. Besides, an increase in the τ_1 value can be associated with an increase in the concentration of these vacancy-like associations.

Independent of the Pr concentration, the obtained positron parameters depend on the atmosphere in which the thermal treatments were performed. Considering the second lifetime component, the τ_2 values obtained for the samples treated in *vacuum* medium were always slightly lower than those obtained for the samples treated in the CO atmosphere; however, they were higher than the values obtained for the samples treated in the O_2 atmosphere. Regarding the associated intensity, the I_2 values obtained for the samples treated in *vacuum* were equal (within the error bars) to that obtained from the samples treated in the CO atmosphere. However, this intensity is higher than those obtained for samples treated in the O_2 atmosphere. Moreover, the behavior of τ_1 shows the same trend as that observed forτ_2. Considering the sample treated in *vacuum* as a reference, it can be concluded that are reductive atmosphere

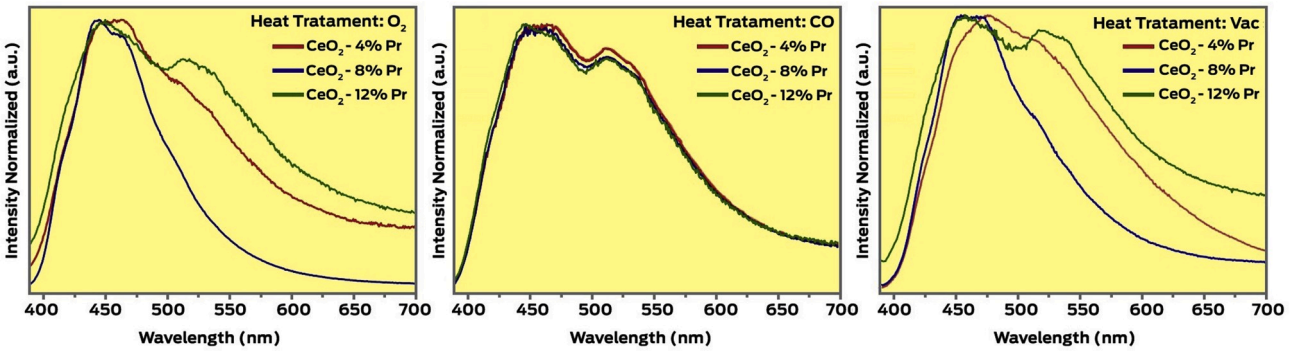

Fig. 4a. PL spectra of CeO_2 doped with 4, 8, and 12% Pr measured at room temperature in O_2, CO atmospheres, and in *vacuum*. Samples subjected to thermal treatment.

(CO) favors the formation of a higher concentration of metal-ion–oxygen vacancy associations (Ce^{3+}-oxygen vacancy and/or Pr^{3+}-oxygen vacancy associations), and a higher concentration of slightly larger VCs compared with the samples treated in the oxidative atmosphere (O_2). Increasing the Pr concentration in the samples amplifies the changes produced in the defect structure by the treatments under distinct atmospheres. Specifically, an increase in the Pr concentration favors an increase in the concentration of both VCs and metal-ion–oxygen vacancy associations. This behavior suggests that oxygen vacancies are formed close to Pr ions.

4.3. PL emissions

Fig. 4a shows the PL spectra of the Pr-doped CeO_2 samples heat treated in O_2 and CO atmospheres and *vacumm* measured at room temperature using a 355-nm Cobolt/Zoukof excitation source.

The spectrum of the Pr-doped CeO_2 sample exhibits a broadband profile that originates from charge transfer occurring between Ce-4f, Pr-5d, and O-2p valence band states. Besides that, this broadband is associated with the structural disorder and vacancies in the lattice that creates energetic levels within the forbidden region and indicates that a multiphoton process occurs as radioactive decay, i.e., emission occurs by several routes [44]. In this work, we related the defects formation due to two factors: i) insertion of Pr on the CeO_2 lattice and ii) heat treatment in different atmospheres, both exert a strong effect on the PL properties and can be related to the non-linear variations on the PL profile [45].

The species$[CeO_8]_o^x$ and $[CeO_8]_d^x$ correspond to structural order and disorder, respectively, which can be assigned as shallow traps visible at high energies as:

$$[CeO_8]_o^x \leftrightarrow [CeO_8]_d^x \quad (1)$$

An organized system is one that has maximum symmetry, i.e., a homogeneous electron density distribution. A disordered system has an inhomogeneous electronic distribution because of variations in bonds, bonding angle, or polarization because of the presence of neighboring clusters. Moreover, the species $[CeO_8]_d^x + [CeO_7.V_O^x] + [CeO_7.V_O^{\bullet}] + [CeO_7.V_O^{\bullet\bullet}]$+ 4f Ce correspond to structural disorder and vacancies, and physically correspond to the previously mentioned deep traps that appear as low-energy signals. In these clusters, the presence of Ce^{+4} species is represented by$[CeO_8]^x$, $[CeO_7.V_O^x]$, and $[CeO_7.V_O^{\bullet}]$ for neutral and paramagnetic clusters, and by$[CeO_7.V_O^{\bullet\bullet}]$for non-paramagnetic clusters. The presence of Ce^{+3} species is represented by $[CeO_4]^{\cdot}$ [46].

Furthermore, a cluster model was proposed to explain the photoluminescent behavior of semiconductors by Longo et al. and Cavalcante et al. [46,47]. In this cluster model, the magnitude and structural order-disorder effects determine the physical properties. The cluster-to-cluster charge transfer (CCCT) process provides a direct insight into the charge carrier dynamics in these materials and suggests that hole polaron trap states localized at oxygen anions are present both, in the bulk and at the surface of the material.

The PL studies highlight the fact that the broadband reaches frequencies ranging from violet to red. The PL response in different regions of the visible spectrum is associated with different routes traveled by the charge carriers before the formation of electron-hole pairs and recombination.

The broadband consists of two most evident emission bands. To better understanding the modifications on the PL profile, the deconvolution of the PL emissions was made using the Voigt area G/L function, as shown in Fig. S6, in SI. This simulates the experimental PL curve with overlapping peaks, and the individual contribution of each component is evaluated by their respective areas and intensities. The PL profiles were adjusted by the addition of three peaks, which have fixed positions in the spectrum. These peaks correspond to blue, green, and yellow, according to the maxima of the components appear. Results shows that the increase of the amount of Pr from 4% to 8% leads a decrease of the red component for heat-treated samples in *vacuum* medium and O_2 atmosphere. However, this red component increases in the samples treated in a CO atmosphere. With the increase of Pr content to 12%, an increase in green-red components is observed in all samples regardless of the atmosphere used in the heat-treatment. Keeping the percentage of Pr fixed, and comparing only the effect of the atmosphere used in the heat treatment, it can be concluded that the heat treatment in a *vacuum* atmosphere generates samples with more pronounced blue components. While the atmospheres of O_2 and CO produce samples with more evident components in the red region. An analysis of the results indicated that the increase in the percentage of Pr and the thermal treatment in different atmospheres generated different defect species, and directly influence the PL properties of the samples.

We attribute this performance to the formation of two negative charges (‘’) in the different doped samples (F4, F8, and F12). The $[CeO_7.V_O^{\bullet}]$and$[PrO_7.V_O^{\bullet}]$, clusters were linked to shallow defects in the band gap energy, which caused a more energetic PL emission in the blue-green region. When the number of$[CeO_7.V_O^{\bullet\bullet}]$complex vacancies increased, they were inserted deeply into the band gap, causing a yellow-red PL emission. The two bands that appeared for the sample treated with CO are associated with vacancy formation and lead to a more significant number of $[PrO_7.V_O^{\bullet\bullet}]$ species.

The oxygen vacancies in a disordered structure $[CeO_8]_d^x$can also be represented as $[CeO_8]_d^x/[CeO_7.V_O^x]$

Complex clusters and can be considered as hole trapping centers. The Ce^{+3} species is intrinsically formed from the disordered clusters that transfer an electron to the ordered cluster$[CeO_8]_o^x$, which represents an adjacent cluster in the net [39–42]. For the Pr-doped samples, the cluster-cluster interactions can be represented as follows:

$$[PrO_8]_o^x \ldots [PrO_7.V_O^x] \ldots \quad [PrO_8]_o^x \rightarrow [PrO_8]_o^{\cdot} \ldots [CeO_7.V_O^{\bullet\bullet}] \ldots [PrO_8]_o^{\cdot} \quad (2)$$

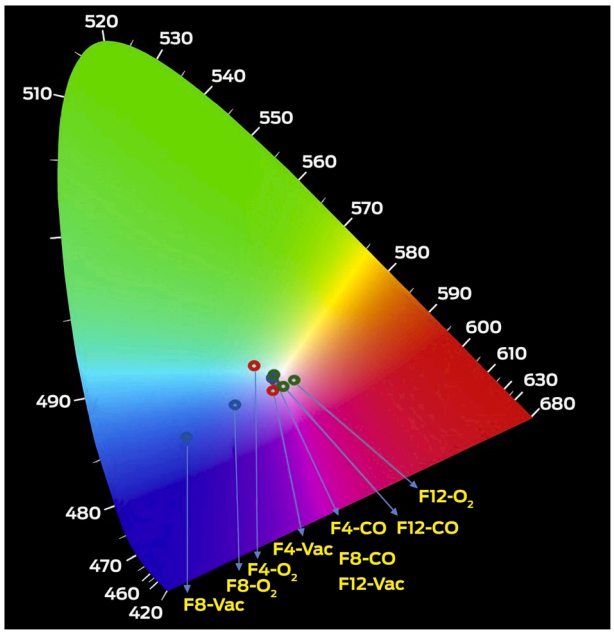

Fig. 4b. CIE chromaticity coordinates of the PL spectra of CeO_2 samples doped with 4, 8, and 12% Pr and submitted to heat treatment in O_2 and CO atmospheres and in *vacuum*.

In Equation (2) the cluster $[PrO_8]_o^{'}$ represent a Pr atom with an electron (') with an adjacent oxygen vacancy. With increasing Pr doping, the concentration of $[CeO_7.V_O^{\bullet\bullet}]$ a species also increases. For all doped samples, the positrons can be trapped in the defects, resulting in no changes in the resistance. These positron trapping sites can be summarized by Equation (3):

$$[REO_8]_o^x \ldots [REO_7.V_O^x] \ldots \quad [REO_8]_o^x \rightarrow [REO_8]_o^{'} \ldots [REO_7.V_O^{\bullet\bullet}] \ldots [REO_8]_o^{'} \qquad (3)$$

where RE represents a RE atom (a Ce or Pr atom, as mentioned above in PALS studies). Based on the PL spectra of the materials, the X- and Y-coordinates were calculated to estimate the emission color of the CeO_2 samples doped with 4, 8, and 12% Pr and submitted to heat treatment in O_2 and CO atmospheres and in *vacuum*. The Commission Internationale de l'Éclairage (CIE) chromaticity diagram was used for this and the results are shown in Fig. 4b.

From the PL spectra shown in Fig. 4a, two typical broadband profiles can be observed. However, based on the CIE chromaticity diagram, can observe that the samples show differences in color emission and that the reflectance was strongly influenced by the Pr percentage and heat-treatment atmosphere. It can be observed that samples containing 4 and 8% Pr (F4 and F8), showed emission in the blue region, whereas samples with 12% Pr (F12) and thermally treated with CO exhibited emission in the white region. We attribute this displacement to the white region to a more substantial amount of vacancies resulting from the higher percentage of Pr dopant. A heat treatment with reducing CO gas and a high percentage of Pr lead to the formation of a more significant number of $[PrO_7.V_O^{\bullet\bullet}]$.

These results indicate that CeO_2 doped with Pr is appropriate for applications in visible lamps, displays, and other optical devices. Moreover, the color of the light can be controlled by varying the amount of Pr and the atmosphere used during heat treatment. Recently, pure white-light-emitting materials have been sough in the optical industry. This is due the following factors: (i) it has been reported that solid-state white-light-emitting devices would reduce global electricity consumption [48], (ii) there is a desire to replace ultraviolet and blue light sources, which are generally more attractive to disease-transmitting insects [49], and (iii) they are environmentally friendly solid-state lighting sources, exhibiting the potential to replace conventionally used incandescent and fluorescent lamps [50].

4.4. Electrical properties in different atmospheres

After the films were heat treated and before they were exposed to CO, in order to select a working temperature for temporal studies, the sensitivity was measured as a function of temperature, as shown in Fig. 5. The electrical resistance measurements were initially conducted as a function of temperature (up to 400 °C) in air and in *vacuum* for samples F4, F8, and F12. As shown in Fig. 5, the sensitivity did not change at temperatures higher than 360 °C.

We represent the relative resistance as R_a/R_V, where R_a corresponds to the resistance of the films when they reach the equilibrium state at different temperatures in an oxygen atmosphere, and R_v corresponds to the electrical resistance when the samples are exposed to *vacuum* (10^{-3} mmHg). As shown in Fig. 5, the ratios R_a/R_V did not change at temperatures higher than 360 °C. In air atmospheres, the interaction of the oxygen species with the clusters can be expressed by the reactions

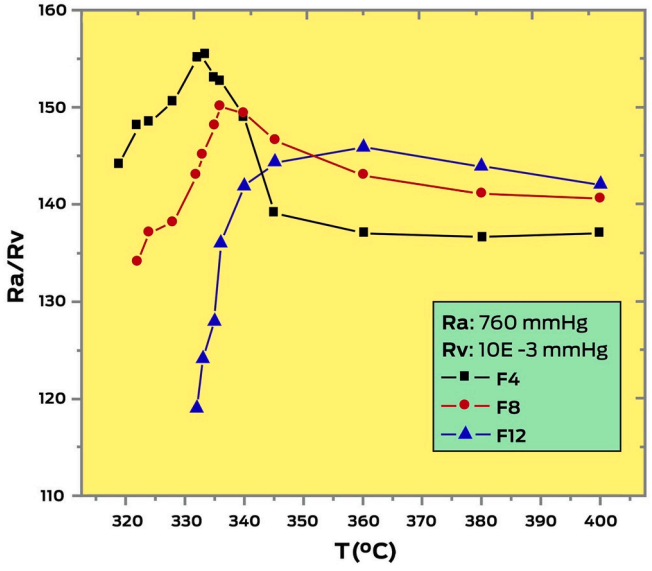

Fig. 5. Relative resistance (R_a/R_V) for the F4, F8, and F12 films as a function of temperature.

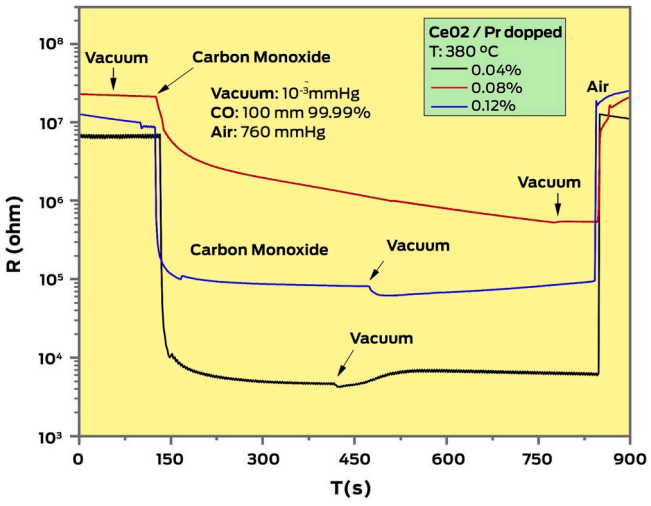

Fig. 6. Resistance as a function of time and atmosphere for Pr-doped ceria films prepared from the nanoparticles synthesized at 100 °C for 8 min by the MAH method under KOH mineralizer.

described in Equation (4):

$$\left[CeO_7.V_O^z\right] + O_2 \rightarrow \left[CeO_7.V_O^z\right]\ldots O_{2(ads)} \quad (4)$$

At this point, it is important to select the predominant paramagnetic species that can act as an attractive center for oxygen adsorption, as stated in Equation (4). We can detect three distinct defects: a diamagnetic neutral defect (V_O^x), a paramagnetic defect ($V_O^\bullet$), and no electrons available at ($V_O^{\bullet\bullet}$). From this analysis, we can consider that the predominant reaction will correspond to Equation (4), followed by O_2 adsorption, and finally by O_2 adsorption. This analysis can be also applied for Pr clusters at the grain surface; however, we consider a net of CeO_2 with a small amount of Pr added. Moreover, we also must consider that different oxygen species can be formed depending on the working temperature. For CeO_2 clusters we can rewrite Equations (5) and (6):

$$\left[CeO_7.V_O^x\right]\ldots O_{2(ads)} \rightarrow \left[CeO_7.V_O^\bullet\right]\ldots O'_{2(ads)} \quad (5)$$

$$\left[CeO_7.V_O^x\right]\ldots O_{2(ads)} \rightarrow \left[CeO_7.V_O^{\bullet\bullet}\right]\ldots O'_{2(ads)} \text{ for } (T > 573K) \quad (6)$$

Equations (13) and (14) represent the formation of ionized paramagnetic oxygen species adsorbed onto the CeO_2 surface. To understand the increase in the electrical resistance caused by doping, we consider the steps in which an electron is transferred from Ce^{+3} to the oxygen adsorbed on the surface. This possible transfer decreases the number of electrons in the 4f states and reduces the electrical conductivity. The conductivity of a sample depends on the number of 4f Ce states occupied by electrons, which corresponds to the Ce^{+3} species (shown in Figs. 5 and 6). Further, increasing the Ce^{+4} concentration decreases the sample conductivity.

After determining the working temperature, time response measurements were conducted while changing the atmosphere from *vacuum* (10^{-3} mmHg) to CO (100 mmHg, 99.99%). When a steady state was reached, the atmosphere was changed from CO to *vacuum*. Once a steady-state was reached again, the *vacuum* was changed back to the dry air atmosphere (at a constant pressure of 760 mmHg for all doped samples).

Fig. 6 shows the time electrical responses (R vs. time) of the films doped with 4, 8, and 12% Pr (labeled as F_4, F_8, and F_{12}, respectively), after changing the atmospheres from *vacuum* (10^{-3} mmHg) to a 99.99% CO atmosphere (100 mmHg in the static-atmosphere chamber). The increase of the sensitivity during the gas injection, the experiments were conducted at a temperature of 380 °C, which was selected from the sensitivity vs. temperature measurements, R_a/R_V, shown in Fig. 5.

When the atmosphere was changed over the course of 2 h from 10^{-3} mmHg (labeled *vacuum*) to CO, a considerable decrease in the resistance was observed for all samples. In this process, initially, CO adsorption occurs. CO adsorption onto a clean semiconductor surface produces an increase in the barrier height and a decrease in the sample conductivity after the adsorption reaction, leading to the formation of CO_2. After CO exposure, one can assume that some of the available Ce^{4+} species in the F4, F8, and F12 samples will react at the surface, resulting in an increase of Ce^{3+} along with an increase in cluster defects($[CeO_7.V_O^\bullet]$ and $[CeO_7.V_O^{\bullet\bullet}]$) that represent the oxygen vacancy species. Sample conductivity increases when CO reacts with the remaining adsorbed oxygen (or with lattice oxygen). The F4 sample exhibited a significant increase in electrical conductivity when exposed to CO. In previous works, we noted that the temperature where the CO reaction takes place is higher than 250 °C [9]. Furthermore, it was shown that once the exposure to $CO_{(g)}$ at 653 K has raised the amount of oxygen vacancy sites for both cases, the interaction of the gas with the film surface can be established for the doped films through the reaction with adsorbed oxygen species on the CeO_2 surface.

The reaction with CO, at temperatures higher than 180 °C, were previously consider in Ref. [51]. For our clusters, processes at T > 573Kcan be also expressed as follows:

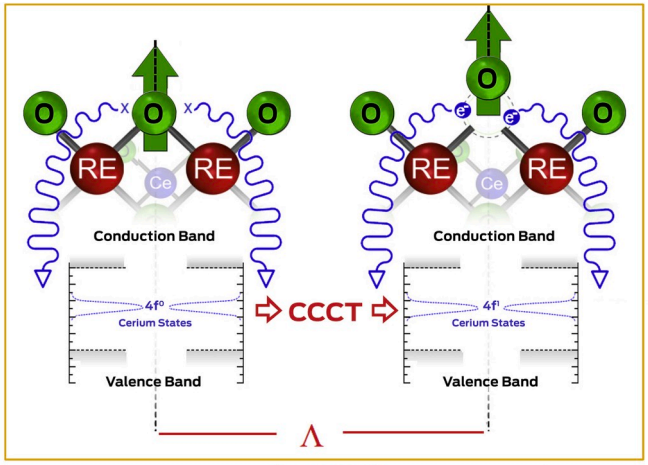

Fig. 7. Band diagram representing the $4f^0$ and $4f^1$ states and the cluster-to-cluster charge transfer process between clusters.

$$\left[CeO_7.V_O^x\right] + \left[CeO_7.V_O^\bullet\right]\ldots O_2 \rightarrow \left[CeO_7.V_O^\bullet\right]\ldots O'_2 + \left[CeO_7.V_O^\bullet\right] \quad (7)$$

$$\left[CeO_7.V_O^\bullet\right]\ldots O'_2 + CO \rightarrow \left[CeO_7.V_O^x\right]\ldots O_2\ldots CO \quad (8)$$

$$\left[CeO_7.V_O^x\right]\ldots O_2\ldots CO_{(ads)} \rightarrow \left[CeO_7.V_O^x\right] + CO_2 + 1/2O_2 \quad (9)$$

where the electron situated in an oxygen species adsorbed onto the surface (O'_2) returns to the net oxygen, reducing the bulk of the material from$[CeO_7.V_O^\bullet]$ to $[CeO_7.V_O^{\bullet\bullet}]$and increasing the electrical conductivity in all samples. In order to study only the interaction between CO and the net oxygen at the surface, we previously exposed the films to *vacuum* atmosphere. Under this condition, we can consider the reaction between CO and the oxygen at the clusters as follows:

$$\begin{aligned} &2[REO_8][REO_8]^x_o\ldots\ [REO_8][REO_8]^x_d\ldots CO \rightarrow [REO_8] \\ &[REO_8]'_o\ldots[REO_7.V_O^{\bullet\bullet}]\ldots[REO_8]'_o + CO_2 \end{aligned} \quad (10)$$

Furthermore, in Equations (7)–(10), we can observe that the CO reaction at the surface liberates two electrons that are available for the 4f states, thus increasing the number of ordered clusters of Ce^{+3}.

In contrast to CO, the interaction of oxygen with grain surfaces produces a reduction in the number of electrons in the 4f states after 850 s, as shown in Fig. 6. This process leaves the 4f state with fewer electrons available for electrical conduction, and a jump in samples resistance was observed.

In previous studies, the hopping process, in which electrons hop rather than tunnel from one atom/molecule to a neighboring one, was proposed [52,53]. It is known that the interactions between electrons and phonons at lattice sites may lead to self-trapping, in which the electrons polarize their neighboring molecules and, thus, become trapped in self-induced potential wells, with the polarization field generated by the moving electron carried through the lattice. This combination can be considered a quasi-particle, generally referred to as a polaron [52, 53]. At this point, considering the PL and PALS results as well as the DFT calculations that showed the presence of defective cluster groups, a CCCT process in a crystal must also be considered as a mechanism for electrical conduction. This group, which consists of more than one type of cluster, is characterized by excitations involving the electronic transitions of 4f states from one cluster to another [46].

Fig. 7 shows a band diagram representing the 4f states and their interaction between cluster aggregations. The Λ parameter represents the distance between cluster groups containing electronic density available for conduction. We define Λ as "quantum gap" for the CCCT process of tunneling or hopping of electrons between clusters, which will

depend on the vacancy concentration. The decrease in the quantum gap increases the tunneling charge transfer between neighboring grouping clusters. According to Kao [54], if the Λ value (i.e., the distance between the two sites) is larger than 10 Å, electrons hop rather than tunnel from one cluster to another. In this case, the probability of a hopping transition can be written as follows:

$$W_H = \upsilon_j \exp(-\Delta Ej / kT) \quad (11)$$

where ΔE_j, is the activation energy, which is E_T- E (Fig. 7), and υ_j is the attempt-to-escape jump frequency [54].

For CeO_2 semiconductors, is essential to consider the possible different charge transfer mechanisms (hopping/tunneling) responsible for electrical conduction at the $4f^1$ states, as represented by the band diagram shown in Fig. 7 [54]. An increase in the energy difference between the E_f and E_{4f} levels increases the sample resistance [9]. At this point, it is necessary to highlight that the band bending and subsequent increases in barrier height and width do not affect the conductivity because of the presence of overlapped potential barriers as a result of the small grain size [55,56]. This is because of the conduction band position at 6 eV (from the valence band and next to 3 eV from the Fermi level, E_F) [9], as shown in the band diagram of Fig. 7. This effect is in good agreement with the theoretical calculations.

The electrical resistances for samples with different Pr content that were thermally treated in *vacuum* were 6×10^6 Ω, 2×10^7 Ω, and 9×10^6 Ω for the F4, F8, and F12 samples, respectively. An increase in the $[CeO_7.V_O^{\bullet\bullet}]$ species is expected, which is reflected by the increase in the initial electrical resistance in *vacuum* for the F8 and F12 samples. In contrast, for F8 and F12, the doping processes increase the electrical resistance $[PrO_8]_o^x$of the samples. When an excess of dopant is formed because of Pr addition, it decreases the Ce^{+3} concentration, as expressed in the following equations:

$$CeO_8][CeO_8]_o^{'} + CeO_7.V_O^x] + 2PrO_8][PrO_8]_o^x \rightarrow CeO_8][CeO_8]_o^x + PrO_8][PrO_8]_o^{'}\ldots CeO_7.V_O^{\bullet}]\ldots[PrO_8]_o^{'} \quad (12)$$

$$[CeO_8]_o^{'}\ldots[PrO_8]_o^x \rightarrow [CeO_8]_o^x + [PrO_8]_o^{'} \quad (13)$$

As shown in PALS analysis, positrons can be trapped into clusters, along with a resistance increase obtained for electrical measurements for F8 and F12. For F12 samples, the positron trapping species are generated because of the double ionized oxygen vacancies generation and they can be represented as follows:

$$PrO_8][PrO_8]_o^{'}\ldots CeO_7.V_O^{\bullet}]\ldots PrO_8][PrO_8]_o^x \rightarrow PrO_8][PrO_8]_o^{'}\ldots CeO_7.V_O^{\bullet\bullet}]\ldots[PrO_8]_o^{'} \quad (14)$$

Table 2
Electrical resistance and sensitivity to CO for samples thermally treated with different gases.

Sample	*Vacuum* (100s) R (Ω)	CO R (Ω)	Sco
F4	6E6	4E3	1500
F8	2E7	8E5	25
F12	9E6	1.5E5	60

Equation (12) corresponds to an increase in mono ionized ($V_O^{\bullet}$) vacancies, represented in the cluster as $[CeO_7.V_O^{\bullet}]$, along with a decrease in Ce^{+3} (species Equation (13)). Moreover, we should consider that Pr atoms can act as acceptors, facilitating the creation of singly ionized vacancies and increasing the electrical resistance at low doping levels. This phenomenon will occur when the Pr doping level is increased for the F8 sample, as increasing the amount of Pr favors the occurrence of doubly ionized oxygen vacancies. It is worth noting that each Pr atom does not necessarily generate an oxygen vacancy. Finally, for high doping levels (sample F12, in Fig. 8), $[PrO_7.V_O^{\bullet\bullet}]$increases, and a mild reduction of the electrical resistance in *vacuum* is observed as a result of the possible conduction via the cluster-to-cluster charge transfer (CCCT) process between the formed Pr f states (shown in DOS diagrams), as a

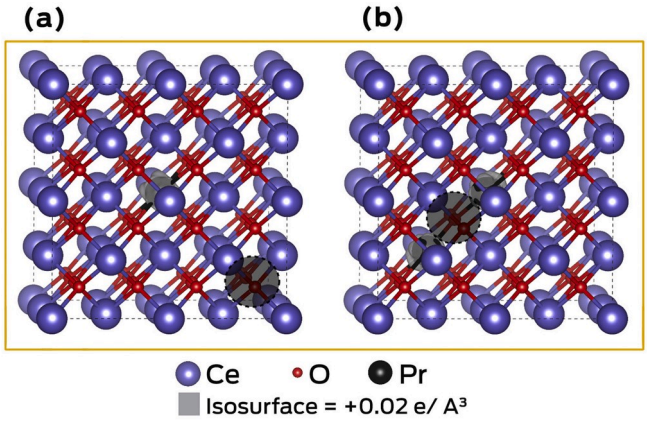

Fig. 9. Calculated oxygen deficiency in Pr-doped CeO_2 geometries. The figure depicts the case of (a) one and (b) two Pr dopant atoms in the CeO_2 lattice with one oxygen vacancy. The blue, red, and black colors represent cerium, oxygen, and Pr atoms, respectively. The oxygen vacancy is indicated by a dark circle. The isosurface used in calculations for both geometries is +0.02 e/A^3. (For interpretation of the references to color in this figure legend, the reader is referred to the Web version of this article.)

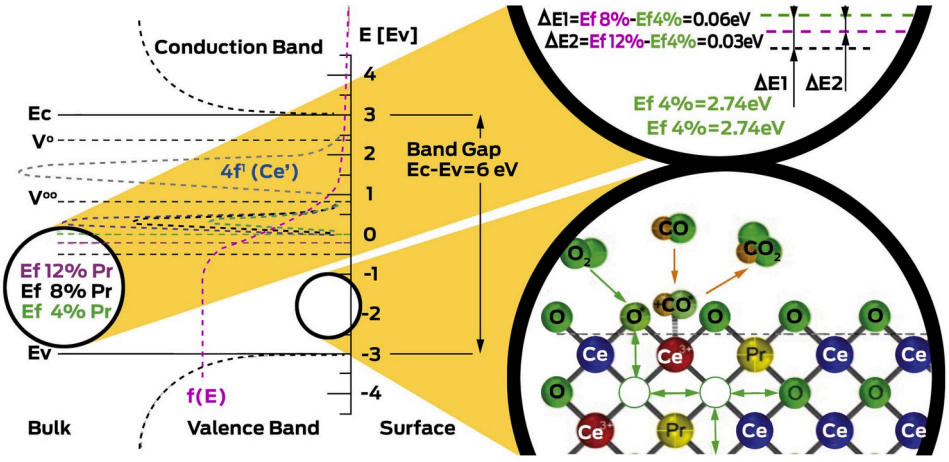

Fig. 8. Band diagram showing the f states responsible for the electric conduction mechanism.

sufficient number of electrons are available for conduction. The increase in the intensity of the 4f Pr states is represented in the band diagram and DOS calculation curves shown in Figs. 7 and 8.

The band gap diagram shown in Fig. 8 illustrates the E_F change when the Pr doping level is increased. These values were acquired for the powders thermally treated in *vacuum* once no changes in the band gap were noted for this condition. The energy difference between the Fermi level (E_F) and the 4f state (E_{4f}-E_F) changes because of doping, therefore reducing the number of electrons available for conduction. The UV–Vis results (Fig. S4, in SI) confirm that samples with 8% Pr, F8 ($E_F = 2.68$ eV), presented a drift of −0.06 eV with respect to the 4% Pr-doped samples, F4 ($E_F = 2.74$ eV). Samples with 12% Pr, F12 ($E_F = 2.71$ eV), presented a drift of −0.03 eV with respect to the 4% Pr-doped samples, F4 ($E_F = 2.74$ eV).

Finally, in Table 2, we summarize the electrical resistance (in Ohms) and sensitivity (S_{CO} and S_{air}) values obtained for samples exposed to CO. It is observed that when doped with Pr, a decrease in the sensitivity after CO exposure (see Table 2) was measured. This behavior can be attributed to an increase in defects, as indicated by PALS and PL experiments for F12 samples for all atmosphere treatments. Then, the number of defects increased with doping and CO exposure. As doping increases, the oxygen vacancies rise in the bulk and at the surface, provoking a decrease in the net oxygen available to react with CO at the surface. In addition, the resistance increases as the Ce^{+3} concentration decreases when the samples are exposed to air, as shown in Fig. 6.

4.5. Theoretical investigations

According to our calculations, the lattice parameter obtained by using the previously mentioned Hubbard correction for the pristine CeO_2 cubic unit-cell was 5.47 Å, while the experimental value obtained by Rietveld refinement was 5.46 Å, deviating by 0.18% from our theoretical investigations. To understand the effects of the electronic properties of the Pr impurity in oxygen-deficient CeO_2, we performed DFT calculations by considering a unit-cell multiplied by two in the three Cartesian directions. To study the effects of Pr doping and oxygen vacancies in CeO_2, we calculated the spin charge density $\Delta\rho = \rho\uparrow - \rho\downarrow$. Fig. 9 shows the most important studied geometries, where the left (right) panel, one (two) Pr atom replaces the ceria atomos in the supercell. Furthermore, one oxygen atom was removed from each cell, distant from and close from the Pr impurity. Cerium, oxygen, and Pr atoms are depicted by blue, red, and black colors, respectively. The gray color represents the used +0.02 e/A^3 isosurface, and the vacancy is indicated by the dark circle (see Fig. 10).

As the defects area ruling factor in the optical and electronic properties of CeO_2, several oxygen vacancies in non-equivalent positions were investigated. For the calculated structures with one Pr dopant atom, we found that the structures with O-vacancy distant from the impurity had a stronger magnetic moment than that in configurations with the oxygen deficiency close to the impurity. However, in the calculations with two doping Pr impurities, the structures with oxygen vacancy between the impurities had a higher magnetic moment than the other geometries tested with different O-vacancy positions in the supercell. The two presented geometries are the most stable ones, even for the calculations in which initial magnetic moments were adopted for the Pr atoms. In addition, the spin-density centered on the Pr dopant depicts the oxidation state Pr^{3+}. The electronic properties were investigated by calculating the local density of states (LDOS) and dividing this by the number of supercell atoms, as shown in Fig. 2. For both structures, the empty f-Ce and d-Ce states present the stronger contributions and the p-O-occupied levels have higher intensity. The f-Pr states shows a higher contribution, where the single peak indicates the localized magnetic moment.

To obtain insights into the charge transfer associated with the O-vacancy and Pr impurity, which changes the Coulomb repulsion between its surrounding atoms, we investigated the effective Bader charges for the calculated geometries (Fig. 9) [57]. The effective Bader charge ($Q^{atom}{}_{eff}$) is calculated as $Q^{atom}{}_{eff} = Z_{val} - Q^{atom}{}_{B}$, (atom = Ce, O, Pr), where Z_{val} is the electron valence, and Q^{atom} is the total charge within the Bader volume. In these calculations, we observe that the O-vacancy plays a fundamental role in the charge transfer calculation. For the geometry with one O-vacancy distant from the Pr impurity, we observed that the effective Bader charge for ceria and oxygen atoms nearest from O-vacancy were 2.79 *e* and −1.53 *e*, respectively. Also, for

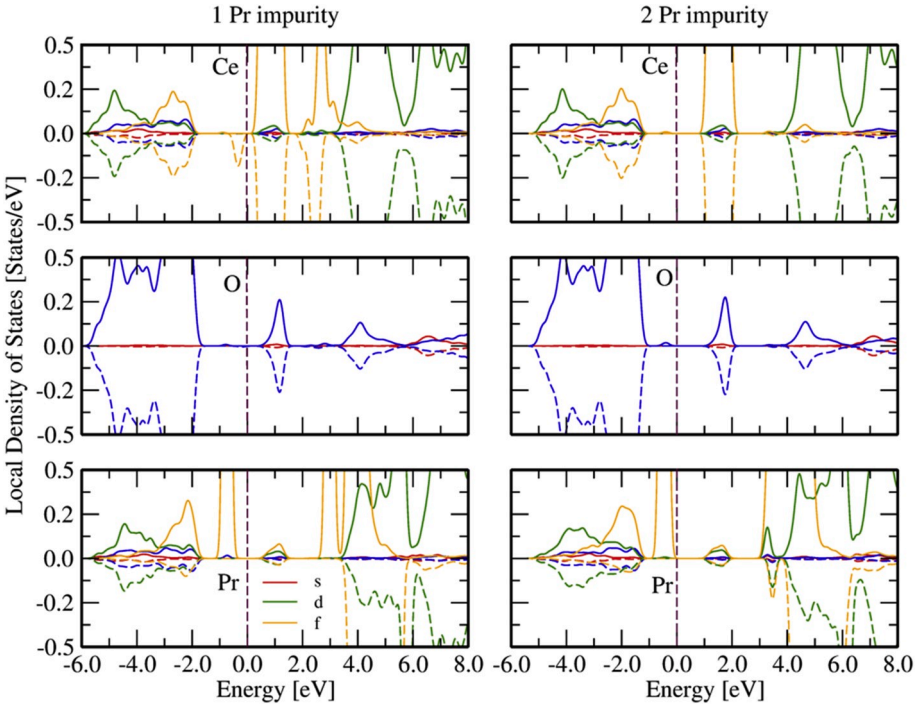

Fig. 10. Local density of states per atom for the calculated geometries shown in Fig. 7. The left (right) panel presents the local DOS per atom in the supercell with one oxygen deficiency and one (two) Pr dopant atom(s).

the geometry with one O-vacancy and two Pr impurities, the effective Bader charge for Ce and O atoms nearest from the O-vacancy were 2.91 *e* and −1.44 *e,* respectively.

In comparison, the average of the effective Bader charges for ceria atoms in the structures with one and two impurity atoms were 2.82 *e* and 2.90 *e,* for oxygen −1.43 *e* and −1.45 *e*, and for Pr impurity(ies) atoms 2.58 *e* and 2.18 *e*, respectively. As expected, the oxygen is the most electronegative atomic specie, suggesting a tendency to accept electrons from the Ce and Pr atoms. A single Pr dopant in the supercell has higher effective Bader charge than in the structure with two impurities. Thus, the position of the oxygen vacancy plays a fundamental role in the charge transfer of CeO_2:Pr based sensors.

5. Conclusions

In this study, crystalline ceria nanoparticles doped with Pr were obtained by MAH growth at 100 °C. The subsequent thermal treatments in different atmospheres resulted in the formation of distinct complex clusters, thereby affecting the PL emission in specific wavelength regions. The PALS results indicated that the defect structures of the samples were composed of large vacancy clusters and small open volume defects with a typical size of a mono vacancy. Furthermore, PALS revealed that the concentration of vacancy-like defects groups present in the samples depended on the atmosphere under which the thermal treatment was performed, and it increased with increasing Pr doping level. The obtained results indicated that the vacancy-like defects were oxygen vacancies surrounded by the negative electronic density of Pr atoms. The electrical measurements conducted in different gas atmospheres demonstrated that Pr-doped CeO_2 acts as an n-type semiconductor. The doped samples presented reversible responses when exposed to oxidants and reductive gases as a result of reactions with surface oxygen. These changes were observed as a decrease in the electrical resistance, which was caused by a decrease in the electron occupation of $4f^1$ states. The number of $4f^1$ electrons decreased because of the decrease in Ce^{+3} concentration during the CCCT process. Theoretical studies revealed the presence of Pr states in the 4f states of Ce atoms. These states were available to receive the $4f^1$ electrons and caused the electrical resistance to increase after doping. If the amount of Pr doping is increased insignificantly, the Pr states can cause a mild increase in conduction as a result of the Pr f state contribution. Vacancies were the main factors that caused Ce^{+3} formation, thereby increasing the number of $4f^1$ electrons available for the subsequent CCCT process. Moreover, we developed a semiconductor nanomaterial that can produce white light and shows great promise for use as a single-material white-light-emitting source. Furthermore, we showed that its structures and light-emitting properties can be tuned systematically.

Declaration of competing interest

The authors declare that they have no known competing financial interests or personal relationships that could have appeared to influence the work reported in this paper.

CRediT authorship contribution statement

Regiane Cristina de Oliveira: Writing - review & editing, Validation. **Luis Cabral:** Software. **Ana Cristina Cabral:** Methodology, Resources. **Priscila Barros Almeida:** Investigation, Resources. **Nicolas Tibaldi:** Investigation, Resources. **Julio Ricardo Sambrano:** Writing - review & editing, Supervision. **Alexandre Zirpoli Simões:** Writing - review & editing, Supervision. **Carlos Eugenio Macchi:** Investigation. **Francisco Moura:** Resources. **Gilmar Eugenio Marques:** Investigation. **Miguel Adolfo Ponce:** Funding acquisition. **Elson Longo:** Funding acquisition, Writing - review & editing.

Acknowledgements

The authors appreciate the support of the Brazilian research financing institutions: Conselho Nacional de Desenvolvimento Científico e Tecnológico (CNPq) Proc. 573636/2008-7 - Fundação de Amparo à Pesquisa do Estado de São Paulo (FAPESP) Proc. 2008/57872-1 and 2019/08928-9; 2018/20729-9; CDMF (Centro de Desenvolvimento de Materiais Funcionais) Proc. 2013/07296-2. This study was financed in part by the Coordenação de Aperfeiçoamento de Pessoal de Nível Superior – Brasil (CAPES) – Finance Code 001. Fundação de Amparo à Pesquisa do Estado de Minas Gerais (FAPEMIG). CEM also acknowledges ANPCyT (Agencia Nacional de Promoción Científica y Tecnológica), grant PICT Proc. 2015–1832. We also acknowledge Enio Longo, for the contribution to image improvement.

Appendix A. Supplementary data

Supplementary data to this article can be found online at https://doi.org/10.1016/j.matchemphys.2020.122967.

References

[1] J. Luňáček, et al., Structure and magnetic properties of synthesized fine cerium dioxide nanoparticles, J. Alloys Compd. 753 (2018) 167–175.
[2] S.C. Erwin, et al., Doping semiconductor nanocrystals, Nature 436 (7047) (2005) 91–94.
[3] L.S.R. Rocha, et al., Novel gas sensor with dual response under CO(g) exposure: optical and electrical stimuli, Phys. B Condens. Matter 536 (2018) 280–288.
[4] R.N. West, Positron studies of condensed matter, Adv. Phys. 22 (3) (1973) 263–383.
[5] K. Singh, et al., *Effect of rare-earth doping in CeO_2 matrix: Correlations with structure, catalytic and visible light photocatalytic properties*, Ceram. Int. 43 (18) (2017) 17041–17047.
[6] M. Prathap Kumar, G.A. Suganya Josephine, A. Sivasamy, *Oxidation of organic dye using nanocrystalline rare earth metal ion doped CeO_2 under UV and Visible light irradiations*, J. Mol. Liq. 242 (2017) 789–797.
[7] A. Rangaswamy, P. Sudarsanam, B.M. Reddy, *Rare earth metal doped CeO_2-based catalytic materials for diesel soot oxidation at lower temperatures*, J. Rare Earths 33 (11) (2015) 1162–1169.
[8] R.C. Deus, et al., Photoluminescence properties of cerium oxidenanoparticles as a function of lanthanum content, Mater. Res. Bull. 70 (2015) 416–423.
[9] P.P. Ortega, et al., Towards carbon monoxide sensors based on europium doped cerium dioxide, Appl. Surf. Sci. 464 (2019) 692–699.
[10] A. Dhara, et al., Effect of lattice distortion in optical properties of CeO2 nanocrystals on Mn substitution by mechanical alloying, J. Alloys Compd. 786 (2019) 215–224.
[11] F. Abbas, et al., *Inhibition of Neuroblastoma cancer cells viability by ferromagnetic Mn doped CeO_2 monodisperse nanoparticles mediated through reactive oxygen species*, Mater. Chem. Phys. 173 (2016) 146–151.
[12] H. Borchert, et al., Electronic and chemical properties of nanostructured cerium dioxide doped withPraseodymium, J. Phys. Chem. B 109 (2005) 10.
[13] Q. He, et al., Effect of praseodymium oxide and cerium–praseodymium mixed oxide in the Pt electrocatalyst performance for the oxygen reduction reaction in PAFCs, J. Appl. Electrochem. 41 (8) (2011) 891–899.
[14] D.-E. Zhang, et al., *Fabrication of rod-like CeO_2: characterization, optical and electrochemical properties*, Solid State Sci. 8 (11) (2006) 1290–1293.
[15] S.-H. Yu, H. Cölfen, A. Fischer, *High quality CeO_2 nanocrystals stabilized by a double hydrophilic block copolymer*, Colloid. Surface. Physicochem. Eng. Aspect. 243 (1–3) (2004) 49–52.
[16] S. Maensiri, et al., *Egg white Synthesis and Photoluminescence of platelike Clusters of CeO_2 nanoparticles*, Cryst. Growth Des. 7 (5) (2007) 5.
[17] A.H. Morshed, et al., Violet/blue emission from epitaxial cerium oxide films on silicon substrates, Appl. Phys. Lett. 70 (13) (1997) 1647–1649.
[18] G. Fei, et al., *Growth and Photoluminescence of epitaxial CeO_2 Film on Si (111) substrate*, Chin. Phys. Lett. 18 (3) (2001) 3.
[19] D.-E. Zhang, et al., *Fabrication of novel threefold shape CeO_2 dendrites: Optical and electrochemical properties*, Chem. Phys. Lett. 430 (4–6) (2006) 326–329.
[20] P.M. Desimone, et al., *Reversible metallization of SnO_2 films under hydrogen and oxygen containing atmospheres*, J. Mater. Sci. 51 (9) (2016) 4451–4461.
[21] F. Schipani, et al., *Study of the oxygen vacancies changes in SnO_2 polycrystalline thick films using impedance and photoemission spectroscopies*, J. Appl. Phys. 116 (19) (2014), 194502.
[22] J. Kansy, Microcomputer program for analysis of positron annihilation, Nucl. Inst. Methods Phys. Res. A 374 (1996) 9.
[23] M.A.P. Nicolas Tibaldi, Pablo Kalafatovich, Hector Asencio, Mariela Paula Desimone, Alexandre Zirpoli Simões, Leandro da Silva Rosa Rocha, Elson Longo da Silva, in: Univesidad Nacional de Mar del Plata (Ed.), Dispositivo de Caracterização Optoeletrônica de Materiais, C.N.d.I.C.y.-C. Univerdade Estadual Paulista Julio de Mesquita Filho, 2017, p. 17. Brasil.

[24] L.S.R.R. Elson Longo, Alexandre Zirpoli Simões, Paula Desimone Mariela, Hector Asencio, Pablo Kalafatovich, Miguel Adolfo Ponce, Nicolas Tibaldi, in: Universidade Estadual Paulista (UNESP) (Ed.), Un dispositivo de CaracterizaciónOptoeletrónica de Materiales, U.N.d.M.d.P.U. Consejo Nacional de Investigaciones Científicas y Técnicas (CONICET), Argentina, 2017, p. 34.
[25] P. Hohenberg, W. Kohn, Inhomogeneous electron gas, Phys. Rev. 136 (3B) (1964) B864–B871.
[26] W. Kohn, L.J. Sham, Self-consistent equations including Exchange and correlation effects, Phys. Rev. 140 (4A) (1965) A1133–A1138.
[27] J.P. Perdew, K. Burke, M. Ernzerhof, Generalized gradient approximation made simple, Phys. Rev. Lett. 77 (18) (1996) 4.
[28] P.E. Blöchl, Projector augmented-wave method, Phys. Rev. B 50 (24) (1994) 17953–17979.
[29] G. Kresse, D. Joubert, Fromultrasoft pseudopotentials to the projector augmented-wave method, Phys. Rev. B 59 (3) (1999) 18.
[30] G. Kresse, J. Hafner, Ab initiomolecular dynamics for open-shell transition metals, Phys. Rev. B 48 (17) (1993) 13115–13118.
[31] G. Kresse, J. Furthmüller, Efficient iterative schemes for ab initio total-energy calculations using a plane-wave basis set, Phys. Rev. B 54 (16) (1996) 18.
[32] S.L. Dudarev, et al., Electron-energy-loss spectra and the structural stability of nickel oxide an LSDA1U study, Phys. Rev. B 57 (3) (1998) 5.
[33] M. Alaydrus, M. Sakaue, H. Kasai, *A DFT+U study on the contribution of 4f electrons to oxygen vacancy formation and migration in Ln-doped CeO_2*, PhysChemChemPhys 18 (18) (2016) 12938–12946.
[34] H.-T. Chen, *First-principles Study of CO Adsorption and Oxidation on Ru-doped CeO_2(111) surface*, J. Phys. Chem. C 116 (10) (2012) 6239–6246.
[35] P.R.L. Keating, et al., *Analysis of intrinsic Defects in CeO_2 Using a koopmans-like GGA+U approach*, J. Phys. Chem. C 116 (3) (2012) 2443–2452.
[36] G. Makov, M.C. Payne, Periodic boundary conditions inabinitiocalculations, Phys. Rev. B 51 (7) (1995) 4014–4022.
[37] J. Neugebauer, M. Scheffler, Adsorbate-substrate and adsorbate-adsorbate interactions of Na and K adlayers on Al(111), Phys. Rev. B 46 (24) (1992) 16067–16080.
[38] C. Macchi, et al., *Vacancy-like defects in nanocrystalline SnO_2: influence of the annealing treatment under different atmospheres*, Phil. Mag. 98 (8) (2017) 673–692.
[39] L. Wang, et al., *Oxygen vacancy clusters essential for the catalytic activity of CeO_2nanocubes for o-xylene oxidation*, Sci. Rep. 7 (1) (2017), 12845.
[40] X. Liu, et al., Oxygen vacancy clusters promoting reducibility and activity on ceria nanorods, J. Am. Ceram. Soc. 131 (2009) 2.
[41] S. Chang, et al., *Shape-dependent interplay between oxygen vacancies and Ag–CeO_2 interaction in Ag/CeO_2 catalysts and their influence on the catalytic activity*, J. Catal. 293 (2012) 195–204.
[42] A.V. Thorat, et al., A positron annihilation spectroscopic investigation of europium-doped cerium oxide nanoparticles, Nanoscale 6 (1) (2014) 608–615.
[43] A. Sachdeva, et al., Positron annihilation spectroscopic studies on Nd-doped ceria, J. Solid State Chem. 178 (6) (2005) 2062–2066.
[44] S. Phoka, et al., *Synthesis, structural and optical properties of CeO_2 nanoparticles synthesized by a simple polyvinyl pyrrolidone (PVP) solution route*, Mater. Chem. Phys. 115 (1) (2009) 423–428.
[45] A.E. Souza, et al., *Photoluminescence activity of $Ba1-xCa_xTiO_3$: dependence on particle size and morphology*, J. Mater. Chem. C 2 (34) (2014) 7056–7070.
[46] V.M. Longo, et al., *Structural conditions that leads to photoluminescence emission in $SrTiO_3$: An experimental and theoretical approach*, J. Appl. Phys. 104 (2) (2008), 023515.
[47] L.S. Cavalcante, et al., *Electronic structure, growth mechanism and photoluminescence of $CaWO_4$crystals*, CrystEngComm 14 (3) (2012) 853–868.
[48] S. Sapra, et al., Bright white-light emission from semiconductor nanocrystals: by chance and by design, Adv. Mater. 19 (4) (2007) 569–572.
[49] T. Longcore, et al., Tuning the white light spectrum of light emitting diode lamps to reduce attraction of nocturnal arthropods, Philos. Trans. R. Soc. Lond. B Biol. Sci. (1667) (2015) 370.
[50] Q. Dai, C.E. Duty, M.Z. Hu, Semiconductor-nanocrystals-based white light-emitting diodes, Small 6 (15) (2010) 1577–1588.
[51] S.M.A. Durrani, M.F. Al-Kuhaili, I.A. Bakhtiari, Carbon monoxide gas-sensing properties of electron-beam deposited cerium oxide thin films, Sensor. Actuator. B Chem. 134 (2) (2008) 934–939.
[52] H.L. Tuller, A.S. Nowick, *Small polaron electron transport in reduced CeO_2 single crystals*, Solid State Commun. 22 (3) (1977) 2.
[53] G.V. SUBBA RAO, et al., Electrical transport in rare-earth oxides, J. Solid State Chem. 2 (1970) 7.
[54] K. Kao, Dielectric Phenomena in Solids, 2004.
[55] M.A. Ponce, C.M. Aldao, M.S. Castro, *Influence of particle size on the conductance of SnO_2 thick films*, J. Eur. Ceram. Soc. 23 (2003) 2105–2111.
[56] M.A. Ponce, M.S. Castro, C.M. Aldao, *Influence of oxygen adsorption and diffusion on the overlapping of intergranular potential barriers in SnO_2 thick films*, Mater. Sci. Eng., B 111 (1) (2004) 14–19.
[57] Bader, R.F.W., Atoms in Molecules A Quantum Theory, ed. O.U. Press. Vol. 1. 1990, Oxford.